Medical Engineering & Physics 32 (2010) 1198–1212

Contents lists available at ScienceDirect

Medical Engineering & Physics

journal homepage: www.elsevier.com/locate/medengphy

Micron particle deposition in a tracheobronchial airway model under different breathing conditions

Kiao Inthavong[a], Lok-Tin Choi[a], Jiyuan Tu[a,*], Songlin Ding[a], Francis Thien[b]

[a] School of Aerospace, Mechanical and Manufacturing Engineering, RMIT University, PO Box 71, Plenty Road, Bundoora, Victoria 3083, Australia
[b] Department of Respiratory Medicine, Eastern Health Box Hill Hospital, Australia

ARTICLE INFO

Article history:
Received 7 April 2010
Received in revised form 23 August 2010
Accepted 24 August 2010

Keywords:
Airway
Particle deposition
Breathing
CFD

ABSTRACT

Effective management of asthma is dependent on achieving adequate delivery of the drugs into the lung. Inhalers come in the form of dry powder inhalers (DPIs) and metered dose inhalers (pMDIs) with the former requiring a deep fast breath for activation while there are no restrictions on inhalation rates for the latter. This study investigates two aerosol medication delivery methods (i) an idealised case for drug particle delivery under a normal breathing cycle (inhalation–exhalation) and (ii) for an increased effort during the inhalation with a breath hold. A computational model of a human tracheobronchial airway was reconstructed from computerised tomography (CT) scans. The model's geometry and lobar flow distribution were compared with experimental and empirical models to verify the current model. Velocity contours and secondary flow vectors showed vortex formation downstream of the bifurcations which enhanced particle deposition. The velocity contour profiles served as a predictive tool for the final deposition patterns. Different spherical aerosol particle sizes (3–10 μm, 1.55 g/cm^3) were introduced into the airway for comparison over a range of Stokes number. It was found that a deep inhalation with a breath hold of 2 s did not necessarily increase later deposition up to the sixth branch generation, but rather there was an increase in the deposition in the first few airway generations was found. In addition the breath hold allows deposition by sedimentation which assists in locally targeted deposition. Visualisation of particle deposition showed local "hot-spots" where particle deposition was concentrated in the lung airway.

1. Introduction

Successful management of asthma is dependent on achieving adequate delivery of drugs into the lungs through integration of the drug formulation and the delivery device performance. The main types of devices in use include pressurised metered dose inhalers (pMDIs) and dry powder inhalers (DPIs). Having been used since the mid 1950 s, the MDI is still the most frequently prescribed inhaler device worldwide, despite the fact that most patients cannot use it correctly [1,2]. The application of pMDIs requires the patient to slowly inhale while actuating the device by pressing down on the top of the canister which releases a single metered dose of the drug formulation (Fig. 1). Usually it is the timing or coordination of the inhalation breath with respect to the actuation that causes the incorrect use. For example patients often fail in producing a continuous inhalation after actuation, or actuation occurs before inhalation or at the end of inhalation [3].

As an alternative, DPIs are designed without any propellant gas and therefore rely on sufficient inspiratory flow to trigger the dosage and deagglomerate the drug powder. This eliminates the need for coordination of inhalation and actuation and instead reliance is now on achieving a high inspiratory flow. The application of DPIs requires the patient to firstly load the drug dosage, then inhale with adequate inspiratory flow, and then a breath hold to allow sedimentation of the drug particle. The requirement of a sufficient inspiratory flow can be problematic for some patients, e.g., children younger than 8 years who had difficulty in generating sufficient inspiratory flow with the *Turbuhaler* [4,5]. Studies into optimising pulmonary drug delivery for patients with asthma have focused on the drug deposition effectiveness in the lung due to the inhaler device design, and delivery method [6,7]. Since particles are transported by the inhaled air, computational studies of the airflow mechanisms and patterns within the airway can provide detailed data that can complement the existing experimental data in order to improve the drug delivery efficiency. It is also apparent that studies of pulmonary drug deposition need to consider unsteady inhalation patterns, not just steady flow rates.

Early studies of airflow in the lung airways include the experimental work by Proetz [8] and Schroter and Sudlow [9]. A few velocity profiles and flow patterns were presented for a double-bifurcation model. In other experimental studies the central airway up to the third generation of the bifurcation was used [10,11]. In these studies, the respiratory flow was treated as a steady or quasi-steady condition based on the Womersley parameter for normal

* Corresponding author. Tel.: +61 3 9925 6191; fax: +61 3 9925 6108.
E-mail address: jiyuan.tu@rmit.edu.au (J. Tu).

1350-4533/$ – see front matter © 2010 IPEM. Published by Elsevier Ltd. All rights reserved.
doi:10.1016/j.medengphy.2010.08.012

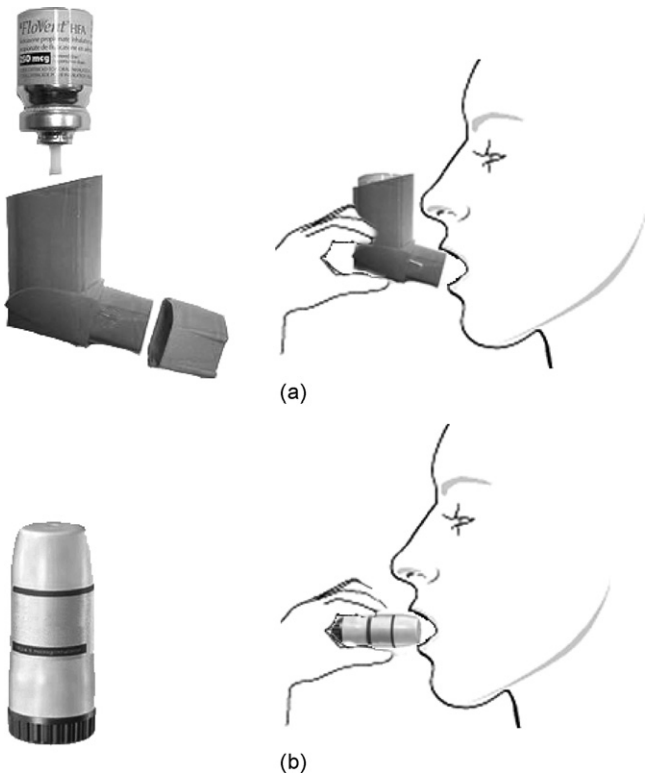

Fig. 1. Pulmonary drug delivery devices. (a) A pressurised MDI showing the canister that holds the drug formulation and its typical delivery technique. (b) DPI which requires sufficient inspiratory flow to deagglomerate the drug formulation.

breathing. Two important parameters that influence the deposition pattern include the local geometry of the tracheobronchial (TB) tree, and the inhalation patterns. Most experimental and numerical studies in the literature on flow in the human airways have been based on simplified, idealised airway models extracted from the early morphological studies by Weibel [12] and Horsfield et al. [13]. van Ertbruggen et al. [14] used irregular dichotomy models based on the morphometric data of Horsfield et al. [13], comparing their numerical results with experimental data [15] in terms of regional deposition efficiency. More recently, studies have explored flow and/or aerosol transport numerically in realistic airway models based on computerised tomography (CT) scanner imaging [16,17]. However these studies used a steady flow rate rather than a sinusoidal breathing pattern.

Micron particle deposition in wall-bounded flows such as the airway is susceptible to inertial impaction, and has often been defined by the inertial parameter $IP = d_a^2 Q$ where d_a is the aerodynamic diameter (μm) and Q is the inhalation flow rate (cm^3/s). Since advection transports the particles through the airway, the particle's inertial property increases proportionally with the flow field velocity, thereby increasing the likelihood of impaction. Gravitational sedimentation of particles is common in the smaller bronchi, the bronchioles, and the alveolar spaces due to the smaller airway diameters and very low airflow velocities. Lippman et al. [18] points out that the effects of sedimentation become significant when the terminal settling velocity of the particles is greater than ~0.001 cm/s, which for unit density spheres is equivalent to a diameter of 0.5 μm. The terminal velocity is reached when viscous and buoyancy forces balance out with gravitational force, and given as

$$U_T = \frac{1}{18}\frac{(\rho_P - \rho_f)}{\mu} g d_a^2 \quad (1)$$

where g is the gravitational force, μ is the fluid dynamic viscosity and ρ is the density. In the TB airway, where the spaces are greater than the alveolar region, sedimentation can be achieved through a pause (breath hold) after inhalation. This action may allow particles that have been transported to a local region to deposit within that region. For MDI devices the aerosol bolus is ejected into the patient until the subject stops breathing. As Matthys [19] points out deposition can be improved by a hold of 5–10 s at a maximal inspiratory level until expiration is started. This study investigates two aerosol medication delivery methods (i) an idealised case for drug particle delivery under a normal breathing cycle (inhalation–exhalation) and (ii) an increased effort during the inhalation (as found for drug delivery through DPIs) with a breath hold. Based on the results of this study, particle deposition patterns caused by the induced airflow patterns can provide a deeper understanding of air-particle dynamics in the tracheobronchial airway and contribute towards improved strategies for more efficient drug delivery.

2. Methods

2.1. Model reconstruction from CT scans

The geometry data was obtained through a computed tomography (CT) scan of the airways of a healthy 53-year-old, non-smoking Caucasian female (164 cm height, 59 kg weight) for the first six generations (from trachea—G0 to bronchi—G5, hence Generation 0–Generation 5). CT scan was performed using a CTI Whole Body Scanner (General Electric). The single-matrix scanner was used in helical mode with 1-mm collimation, a 40-cm field of view (FOV), 120 kV peak and 200 mA. At baseline, 2 cm axial length of lung caudad to the inferior pulmonary ligament was scanned during a single full inhalation total lung capacity breath hold (FEV1 was measured at 2.31 L), which yielded 146 contiguous images (slices in transverse direction, Z) of 1-mm thickness with voxel size 0.25 mm × 0.25 mm × 1 mm. Then, the CT data was fed into an airway tree geometrical reconstruction software that can identify the airway lumen in the CT image (Pulmonary Workstation, VIDA Diagnostics, Iowa). The segmentation step is a semi-automated system which segments a 3D data set by performing 2D analysis. The segmentation algorithm is a region-based growing method where the growth of the foreground region and growth of the background region compete against each other (Fig. 2). The accuracy/fidelity of the algorithm has been published in Tschirren et al. [20]. The segmentation extraction was performed by an expert medical practitioner to interactively manipulate parameters such as region-grow thresholds using visual examination on the slice by slice basis. This inevitably leads to some user specific variability which is unavoidable. For example, the threshold setting in Hounsfeld Units (HU) was defined with an upper and lower bound which then selects the pixels in the image which have a value within that range. This setting is thus dependent on the expertise of the user since the threshold setting is used to delineate a wall region from its mucus lining. In this instance, the lining of mucus was determined by measuring pixels that contained a different colour to the main airway mask found at the interface region between the airway wall and the actual airway. On average the mucus thickness of the airway was estimated to be 0.7 mm, which was included as part of the airway. The 3D model was then converted to IGES (Initial Graphics Exchange Specification) file. Based on the IGES file, SolidWorks 2005 was used to segment the model in terms of trachea, bifurcation and outlet. Finally, face, volume, mesh and extension tubes at outlets were created using GAMBIT 2.2 and a mesh file was produced, which was then read into FLUENT 6.2.

2.2. Geometry generation

The reconstructed model of the human TB airway is depicted in Fig. 3a which consists of the first six generations from the trachea

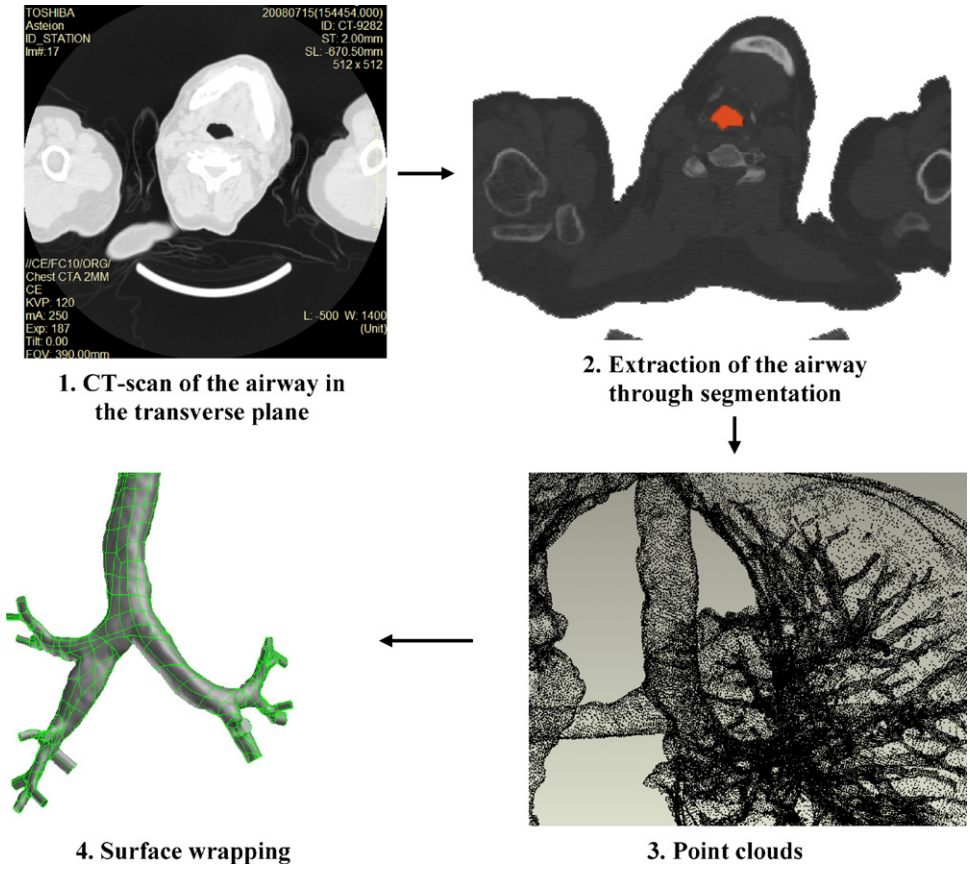

Fig. 2. Steps in the reconstruction of the airway from CT scans to a 3D surface model.

down to the fifth generation. The outlets were artificially extended downstream given by, $L_{extension} = 0.05\mathrm{Re}D$ to allow fully developed profiles at the exits to avoid any reverse flow that may be caused, due to an abrupt end to the flow field. The trachea was also extended upstream by the same fully developed length ($L_{extension}$) thus allowing the flow to be fully developed by the time it reached the tracheal inlet. Fig. 3b illustrates the bifurcation regions used for measuring deposition fraction and its identification scheme. Geometric measurements of the airway model were taken by measuring selected vertex points found at the relevant cross-section in the CFD software. Branch measurements of the length, diameter and bifurcation angles (where applicable) are given in Table 1 with comparative

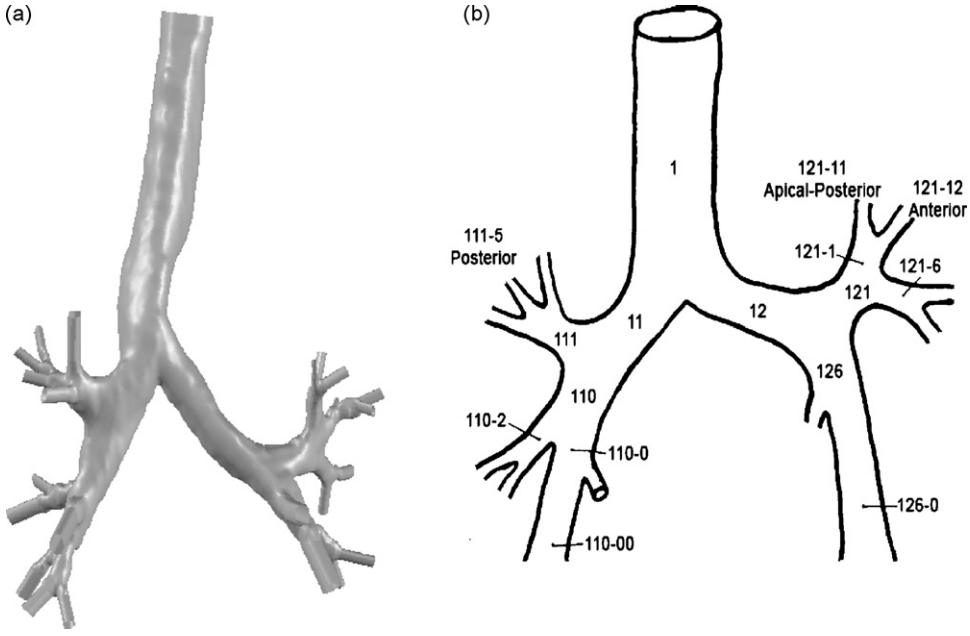

Fig. 3. Realistic six-generation airway lung model (a) the front view of the studied 3D airway model; (b) schematic of the airway model with branch identification for particle deposition analysis. The airway identification number (AIN) is based on the scheme by Mortensen et al. [23].

Table 1
Geometric measurements of the CFD model compared with measurements by Zhou and Cheng [21] and Sauret et al. [22].

	Description	AIN	Length (mm)			Diameter (mm)			Bifurcation angle (°)	
			CFD	ZC	Sau	CFD	ZC	Sau	CFD	ZC
First generation	Trachea[a]	1	105	74		16	16	15.2		
Second generation	Right main B.	11	15	3	21	16	12	12.2	61	35
	Left main B.	12	46	18		10	7			
Third generation	Right U.L. B.	111	11	15	17	14	6	9.5	90	84
	B. Intermedius	110	32	16		13	9			
	Left U.L. B.	121	15	6		10	7		17	35
	Left L.L. B.	126	12	21		10	3			
Fourth generation	Right U.L. post. B.	111-5	6	9		6	5		18	80
	Right U.L. ant. B.	110-2	14			8			54	
	Right L.L. B.	110-0	8	9	14	11	8	6.7		35
	Upper division Left L.L.	121-1	6			7				
	Lower division Left L.U.	121-6	10	7		9	6		45	50
	Left L.L. basal B.	126-0	12	7		9	6			78
Fifth generation	–	111-53	7		11	5		3.4	33	
	Right L.L. basal B	110-00	13			8			54	
	Left U.L. ant. B	121-12	7			6			42	
	Left U.L. apical-post. B	121-11	7			8				
	Left L.L. post. basal B	126-05	11			8			46	
Sixth generation	–	110-002	12		9	7		2.9	35	
	–	121-110	7			6				
	–	121-121	6			4			11	

Note: CFD, CFD model measurement; ZC, Zhou and Cheng [21] measurements; Sau, Sauret et al. [22] measurements. B., bronchus; U.L., upper lobe; L.L., lower lobe.
[a] Trachea has a slight bend caused by the presence of the aortic vessel.

data from Zhou and Cheng [21], and Sauret et al. [22]. The airway identification scheme is based on the method presented by Mortensen et al. [23] which assigns an airway identification number (AIN) to a specific airway. The initial model underwent mesh refinement by cell adaption techniques that included refining large volume cells, cells that displayed high velocity gradients, and near wall refinements. Velocity profiles were compared between each subsequent model until the profiles remained the same and hence became independent of the grid size. The final model had a mesh size of 1.3 million cells (Fig. 4a).

2.3. Breathing conditions

The inhalation requirements differ for the use of a DPI in comparison with an MDI. Broeders et al. [24] showed that dose emissions from the *Diskus* brand DPI operated effectively with a peak inspiratory flow (PIF) of 30 L/min, however for the *Turbuhaler* brand the DPI was operational at 30 L/min and was optimal at a PIF of 60 L/min. For some DPIs that are low resistance devices (*Spinhaler* and *Rotahaler*), the operational PIF is 90 L/min [25]. From these conditions an idealised sinusoidal breathing condition with a PIF of 90 L/min (i.e., 1.5 L/s) over a 2-s period is used. This breathing condition is labelled as Case 1 (Fig. 4b and Table 2) which may represent inhalation for operating a DPI device where a patient inhales with exertion to achieve 2 L in 2 s and then holds the breath for 2 s for the drug particles to settle. In this breathing method, the aerosol is introduced into the airway system during the first 0.805 s of inhalation (equal to 400 mL inhaled). This was chosen so that the tidal volume is the same as the second breathing case which exhibits a smaller PIF. The second breathing condition, labelled Case 2 will be the benchmark case where the patient breathes in and out for 5 breaths in 2-s cycles with a tidal volume of 400 mL; hence 10 s of breathing and total volume of inhaled air is 2 L as well. However, only one breathing cycle was used for the analysis in this study. This was mainly because one breathing cycle was enough to achieve statistically independent results of deposition efficiency (percentage of total particles entered) and hence the deposition pattern would have been similar irrespective of how many breaths were numerically simulated. In this breathing method, the aerosol is introduced into the airway system during throughout the entire

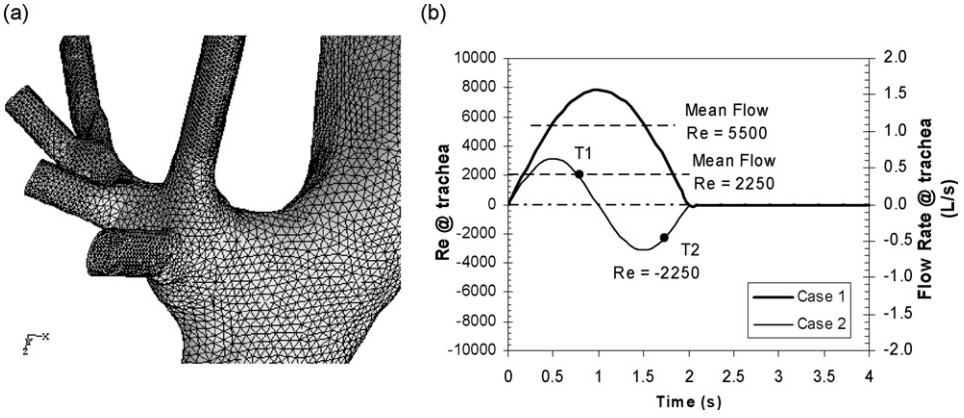

Fig. 4. (a) Finite volume mesh (b) the flow input waveforms used in this study. The times $T1 = 0.82$ s and $T2 = 1.74$ s are chosen at the flow rate producing Re = 2250 during inhalation and at exhalation.

Table 2
Flow and particle transport details.

Method	Case 1	Case 2
Mean respiratory rate (Q, L/min)	66	24
Mean Reynolds number[a] at inlet	5500	2250
Inspiratory capacity (mL)	2000	400
Time ratio of inspiratory phase (t_{in}/t_{total})	0.5	0.5
Frequency (cycle/min)	15	30
Peak inspiratory and expiratory Reynolds number at inlet	8649	3459
Particle diameter (d_p, μm)	5 (plus 3, 7 and 10)	
Particle density (ρ_p, kg/m^3)	1550	
Mean Stokes number[b] at inlet for d_p = 5 μm	0.03861	0.01930

Note: U, D, ρ_{air}, μ, ρ_p and d_p are the mean velocity, inlet diameter, air density, air dynamic viscosity, particle density and particle diameter, respectively.
[a] Reynolds number, $\mathrm{Re} = UD\rho/\mu$.
[b] Stokes number, $\mathrm{St} = \rho_p d_p^2 U/18\mu D$.

inhalation (400 mL tidal volume during 1 s). The input waveform for Case 2 is defined by

$$\dot{m} = 3.91\sin(\pi t), \tag{2}$$

where $\dot{m}$ is the mass flux, and t is the time.

The major differences between Case 1 and Case 2 are not only the different flow rate and frequency, but also that there is no exhalation phase in Case 1. The absence of exhalation in Case 1 is applied in this instance to highlight the effects of allowing the particles to settle by having a user hold their breath as suggested by Matthys [19]. Therefore in the breathing condition simulation of Case 1 applies 2 s of inhalation and 2 s of breath holding, instead of exhalation. Since no exhalation is considered, the results of Case 1 do not reflect the fraction of particles that remain airborne at the end of the breath hold period which may be deposited in the upper bronchial airways upon exhalation. In contrast, Case 2 simulates an entire breathing cycle. During the exhalation phase a new set of particles are released from the outlets (for 1-s duration) to account for some particles that are suspended in the air past the fifth generation. These particles are tracked in addition to any particles suspended inside the computational domain (airway geometry) during the inhalation phase. The number of new particles at the outlet is equal to the number of particles that escaped and therefore neglects any particle-airflow dynamics and deposition downstream of the fifth airway generation. In reality some particles will deposit downstream and therefore the actual number of new particles being introduced at the outlet cannot be known without a full lung model. Instead the number of particles becomes a representative value which is acceptable given that the discrete phase modelling approach uses the parcel approach where a single particle is a statistical representation of a fixed number of physical particles. This means that the number of particles per parcel will be constant along its trajectory and the number of particles per parcel is determined by the total mass flow rate of the disperse phase distributed between and the number of parcel traces. The particles at each outlet are assumed to be uniformly distributed over the area of the outlet. The unsteady breathing condition was simulated by a sinusoidal waveform in both cases and applied at the inlet through user-defined functions in FLUENT 6.2. For this study the method from previous studies in the literature [26–29] is used here, where a parabolic inlet profile from an extended trachea is used. In a recent numerical study by Li et al. [30], it was found that the type of velocity inlet condition and existence of cartilaginous rings influences the airflow field; however, their impact is less important in comparison with the variations in the upper airway geometry, e.g., branch curvature. One cycle without releasing particles was also simulated to avoid start-up effects on the air-particle flow fields before the actual simulation took place. Particles were released at each time step (0.005 s) according to the preset particle flow rate which was assumed to be 300 micrograms per second (μg/s). A parabolic profile of particles was injected matching the fully developed inlet profile due to the exclusion of the larynx. Zhang et al. [31] demonstrated that different flow rates and particle sizes would affect the particle deposition in the trachea after the glottis. The role of the larynx in producing a laryngeal jet and its effect on the downstream flow field and subsequent particle deposition have been published [32–34]. In this study the absence of the laryngeal jet is expected to produce an underprediction of the deposition efficiency in the first bifurcation at the carina. However deeper into the lung airways the effects of the laryngeal jet diminishes and eventually becomes negligible. The parameters of the respiratory and associated particle characteristics are summarized in Table 2. During the exhalation phase particles are re-introduced into the airway from the outlets (for 1-s duration). This idealised condition is used as it allows comparisons for the deposition efficiencies purely from the effects of the breathing cycle for the given limited geometry (six generations). In reality the fate of the particles that initially pass through the outlets is unknown and a fraction of these particles that did not deposit may re-enter the airway. Instead the particle concentration at each outlet is assumed to be proportional to the area of the outlet.

Particles in the range of 3–10 μm were used to match the deposition data found in the literature. This particle size range is also typical of those particles that are likely to reach the TB airways from inhalation [35]. Although 10 μm particles are highly susceptible to early impaction in the upper respiratory region (i.e., mouth, larynx, etc.), for quantitative demonstration of local deposition, 5 μm and 10 μm particles are analysed which reflects the deposition efficiencies of two highly different Stokes numbered particles. Particle deposition fractions were recorded for the first two bifurcation regions. The demarcation lines that define the bifurcation regions are shown in Fig. 5 which are based on the regions found in the experimental work of Zhou and Cheng [21]. The deposition fraction in the first generation is compared with experimental data [21] and several theoretical models of Cai and Yu [36] and Cheng et al. [37]. All collected data were plotted against the local Stokes number for the first three bifurcations where the local Stokes number is defined as

$$\mathrm{St} = \frac{\rho_p d_p U_{local}}{18\mu D_{local}} \tag{3}$$

The local velocity and diameter are taken as the average velocity and diameters within the specific airway branch as identified in Table 1.

2.4. Numerical equations

The low Reynolds number (LRN) k–ω model is used to capture the airflow structures in the laminar to turbulent flow regimes for internal flow [38–40]. The airway tree was constructed from unstructured tetrahedral cells and the commercial CFD code, FLUENT was used to predict the continuum gas phase flow under

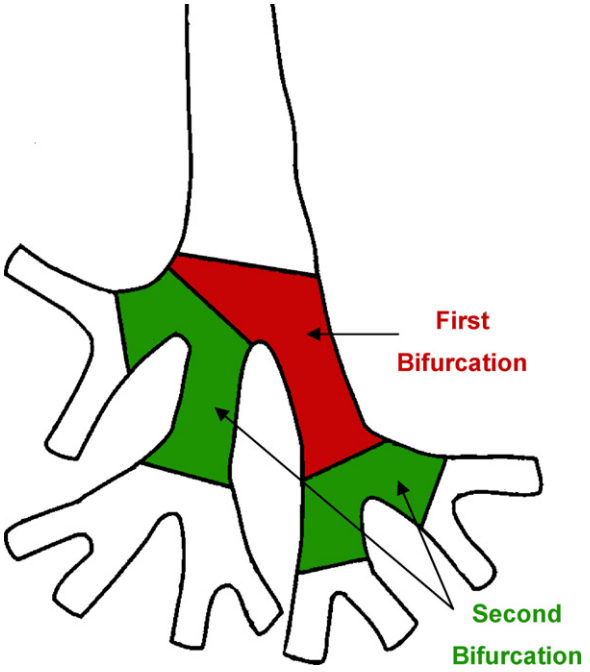

Fig. 5. Schematic of the upper respiratory airway replica adapted from Zhou and Cheng [21] showing the regions for the first and second bifurcation regions.

unsteady-state, isothermal, and incompressible conditions through solutions of the conservation equations of mass and momentum. These equations in Cartesian tensor notation are

Continuity equation:

$$\frac{\partial \bar{u}_i}{\partial x_i} = 0 \tag{4}$$

Momentum equation:

$$\frac{\partial \bar{u}_i}{\partial t} + \bar{u}_j \frac{\partial \bar{u}_i}{\partial x_j} = -\frac{1}{\rho}\frac{\partial p}{\partial x_i} + \frac{\partial}{\partial x_j}\left[\mu\left(\frac{\partial \bar{u}_i}{\partial x_j} + \frac{\partial \bar{u}_j}{\partial x_i} - \frac{2}{3}\delta_{ij}\frac{\partial \bar{u}_k}{\partial x_k}\right)\right] + \frac{\partial}{\partial x_j}\left(-\rho\overline{u'_i u'_j}\right) \tag{5}$$

The Reynolds stresses are related to the mean velocity gradients as

$$-\rho\overline{u'_i u'_j} = \mu_T\left(\frac{\partial u_i}{\partial u_j} + \frac{\partial u_j}{\partial u_i}\right) - \frac{2}{3}\left(\rho k + \mu_T\frac{\partial u_k}{\partial u_k}\right)\delta_{ij} \tag{6}$$

Turbulence kinetic energy (k) equation:

$$\frac{\partial k}{\partial t} + \bar{u}_j\frac{\partial k}{\partial x_j} = \tau_{ij}\frac{\partial \bar{u}_i}{\partial x_j} - \beta * k\omega + \frac{\partial}{\partial x_j}\left[(\nu + \sigma_k\nu_T)\frac{\partial k}{\partial x_j}\right] \tag{7}$$

Specific dissipation rate (ω) equation:

$$\frac{\partial \omega}{\partial t} + \bar{u}_j\frac{\partial \omega}{\partial x_j} = \alpha\frac{\omega}{k}\tau_{ij}\frac{\partial \bar{u}_i}{\partial x_j} - \beta\omega^2 + \frac{\partial}{\partial x_j}\left[(\nu + \sigma_\omega\nu_T)\frac{\partial \omega}{\partial x_j}\right] \tag{8}$$

The symbols in the above equations, t, ρ, p, ν, ν_T, τ_{ij}, k and ω, are time, density, pressure, kinetic molecular viscosity, turbulent viscosity, Reynolds stress tensor, turbulence kinetic energy, and specific dissipation rate, respectively. ν_T is given as $\nu_T = f_\mu k/\omega$, and the function f_μ is defined as $f_\mu = \exp[-3.4/(1 + Re_T/50)^2]$ with $Re_T = \rho k/(\mu\omega)$ and μ being the dynamic molecular viscosity ($\mu = \rho\nu$). C_μ, α, β, β^*, σ_k, and σ_ω are turbulence constants [41]: $C_\mu = 0.09$, $\alpha = 0.555$, $\beta = 0.8333$, $\beta^* = 1$ and $\sigma_k = \sigma_\omega = 0.5$.

For a low volume fraction of the dispersed particle phase, an Eulerian–Lagrangian approach can be used. Trajectories of individual particles are tracked by integrating a force balance equation on the particle. The force balance equation is given as

$$\frac{du_i^p}{dt} = F_D\left(u_i^g - u_i^p\right) + \frac{g(\rho_p - \rho_g)}{\rho_p} + S_i \tag{9}$$

The drag force per unit particle mass is $F_D\left(u_i^g - u_i^p\right)$ and F_D is given by

$$F_D = \frac{18\mu_g}{\rho_p d_p^2}\frac{C_D Re}{24} \tag{10}$$

Re is the particle Reynolds number, which is defined as

$$Re \equiv \frac{\rho_g d_p\left|u^p - u^g\right|}{\mu} \tag{11}$$

where u^g, u^p, μ, ρ_g, ρ_p and d_p are gas (air) velocity, particle velocity, molecular viscosity of the fluid, fluid density, particle density and particle diameter, respectively. The drag coefficient, C_D, is evaluated from an experimental-fitted expression [42]. One-way coupling is assumed between the air and particle flow fields and the interaction between particles is also neglected because the particle flow is dilute (i.e., the volume fraction of the particles is <0.1%). S_i is additional forces that include the Saffman lift force, pressure force, buoyancy force, virtual mass effect and Basset force. Solid aerosols such as drug particles or toxic fibres are generally in the micron size range and typically far denser than air, causing terms that depend on the density ratio, such as those in S_i to be negligibly small. The number of particles tracked was checked for statistical independence. This was determined by increasing the number of particles inhaled (5 μm was used) and increasing the particle injection time step until the total deposition efficiency within the airway became statistically independent of the total number of particles injected. Individual deposition fraction within a branch is defined as the ratio of the number of particles depositing in a branch to the total number of particles injected. The number of particles introduced into the airway was 1539 particles per time step. For Case 1 breathing this equated to 247,779 particles during the first 0.805 s of inhalation, while for Case 2 breathing this equated to 307,800 particles during the 1 s of inhalation.

The turbulent dispersion of the particle trajectory equations can be modelled through the stochastic Eddy Interaction Model (EIM). The effect of instantaneous turbulent velocity fluctuations on the particle trajectories for each time step was calculated after a converged flow fields was achieved. The instantaneous fluctuating velocity components u_i' are obtained from a Gaussian probability distribution, so that

$$u'_i = \zeta\sqrt{\overline{u_i'^2}} \tag{12}$$

where ζ is a normally distributed random number, and the remaining right-hand side is the local root mean square (RMS) velocity fluctuations which is obtained through the following relation:

$$\sqrt{\overline{u'_i{}^2}} = \sqrt{2k_g/3} \tag{13}$$

This implies isotropic fluctuations in all three dimensions which produce significantly higher fluctuation values in the normal direction (v') at no-slip surfaces such as wall-bounded flows. As a result, particle deposition is much higher than expected for small Stokes numbered particles. Several authors have applied near wall corrections to damp the fluctuations damping functions at the near wall [43,44]. In a previous study by the authors [45], a hybrid method that involves the turbulent dispersion for larger particles and a mean-flow tracking (no turbulent particle dispersion) for smaller particles was used and is adopted here. In this model it was found that the EIM model was valid for particles with an inertial parameter $\left(IP = d_a^2 Q\right)$ above 10,000. For particles with an IP < 10,000 the

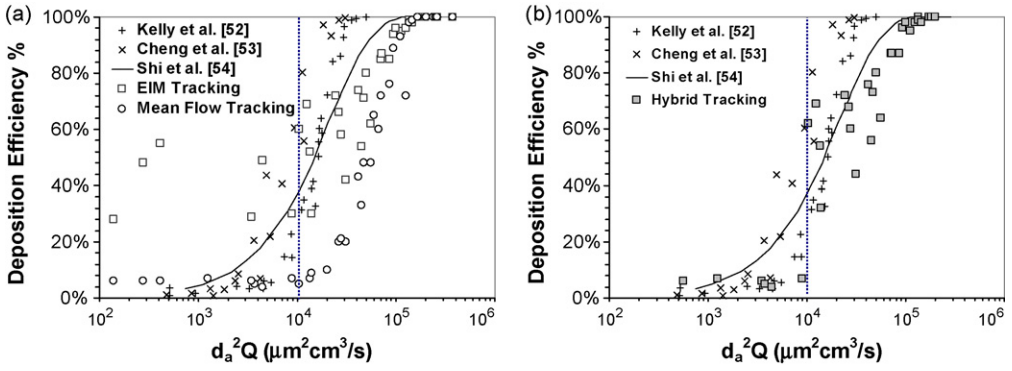

Fig. 6. Deposition efficiency testing for monodisperse particles released into a nasal cavity with flow rate between 10 and 30 L/min airflow using a (a) the EIM and mean-flow tracking, and (b) a combination of the two tracking methods in a hybrid tracking scheme. The switch between the EIM and mean flow tracking occurs at $d_a^2Q = 10,000$. Comparison data comes from experimental and numerical data found in the literature [52–54].

EIM overpredicted the particle deposition, and instead the mean-flow tracking was used (Fig. 6). This idealised system improves the predictions of particle deposition in comparison with experimental data.

The unsteady governing equations were solved in FLUENT 6.2 (Ansys Inc.) using the segregated method with implicit formulation. The advantage of the fully implicit scheme is that it is unconditionally stable with respect to time step size. The SIMPLEC algorithm with under-relaxation was selected for the pressure–velocity coupling. The convective terms of the transport equations were all discretised using second-order-upwind scheme in order to obtain sufficiently accurate solutions. For stable and accurate iterative process, the relaxation factors for momentum and pressure were set to 0.5 and 0.2 respectively. In addition, the residual values of the governing equations and the transport equations were all set to converge at 10^{-4} with a time step size of 0.005 s for both simulation cases. All calculations were performed on a Dell P4 3-GHz PC workstation with 2 GB of RAM. A typical run time for fluid flow and particle transport simulations was approximately 96 h.

3. Results

3.1. Airflow analysis

Axial and secondary velocity profiles were obtained throughout the six-generation airway model under the two breathing conditions (i.e., Case 1 and Case 2). For brevity, only the velocity profiles for Case 2, which includes the inhalation and exhalation phase, are discussed (Fig. 7) as the flow conditions are comparable with existing experimental data [46]. For Case 1 which exhibits an increased exertion, it is expected that the profiles will retain the general profile shape but be more exaggerated in terms of the skewed profiles and the magnitudes. Normalised axial velocity profiles for inspiration and expiration were plotted which showed generally good agreement with experimental results in terms of the main characteristic flow features. Discrepancies are found at S2, S5, and S8 where the computational model cannot capture the sharp gradients in the profiles at these cross-sections. The locations of these discrepancies appear in the daughter branches, immediately after the bifurcation of the parent branch. In these regions, complex flow patterns have been reported [47] which is difficult to match. In addition the Reynolds number matching in the trachea was not perfect (2250 compared with 2040 for Menon et al. [46] and CFD simulation respectively) due to the selection of the simulated inhalation condition.

For *inspiratory flow* (Fig. 7b), the velocity profile at S1 exhibited a skewed parabolic shape caused by the bend in the trachea region. The flow splits at the first bifurcation and the profiles become skewed towards the inner walls of the first bifurcation as shown at S2 and S3. The profile at S2 was more skewed than S3 because the right main bronchus has a more acute branching angle than the left main bronchus. The flow begins to recover, and downstream in the left main bronchus the profile at S4 is less skewed than at S2. Similar asymmetric velocity fields are found at S5 and S6, where the

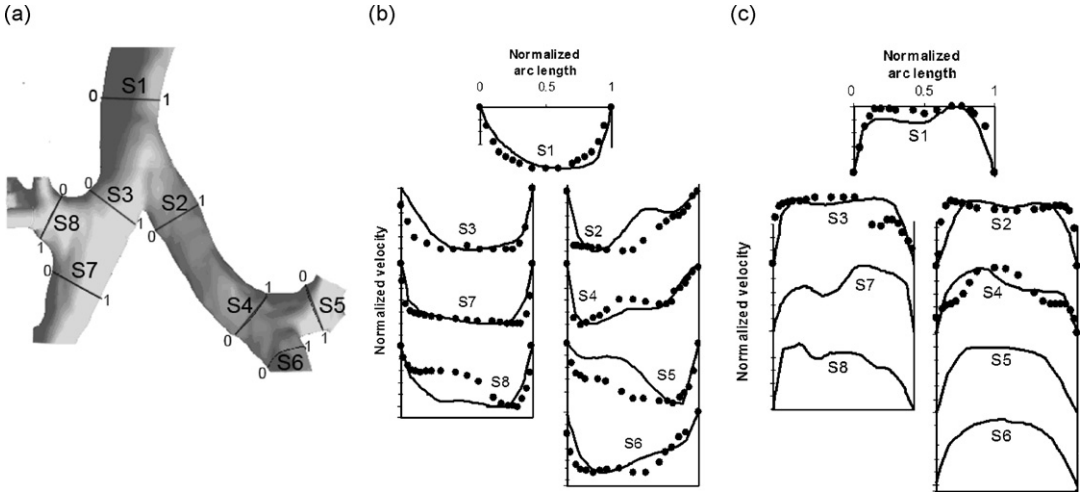

Fig. 7. (a) View of stations (S) for axial velocity. Letter, S represents station with thinner line. Slices are labelled alphabetically (A–A′ to G–G′) used for velocity contours and secondary flow vectors. Normalised axial velocity profile for (b) inhalation and (c) exhalation at Re = 2250, plotted as a function of the normalised arc length. The experimental data of Menon et al. [46] are plotted as (●) for the corresponding stations.

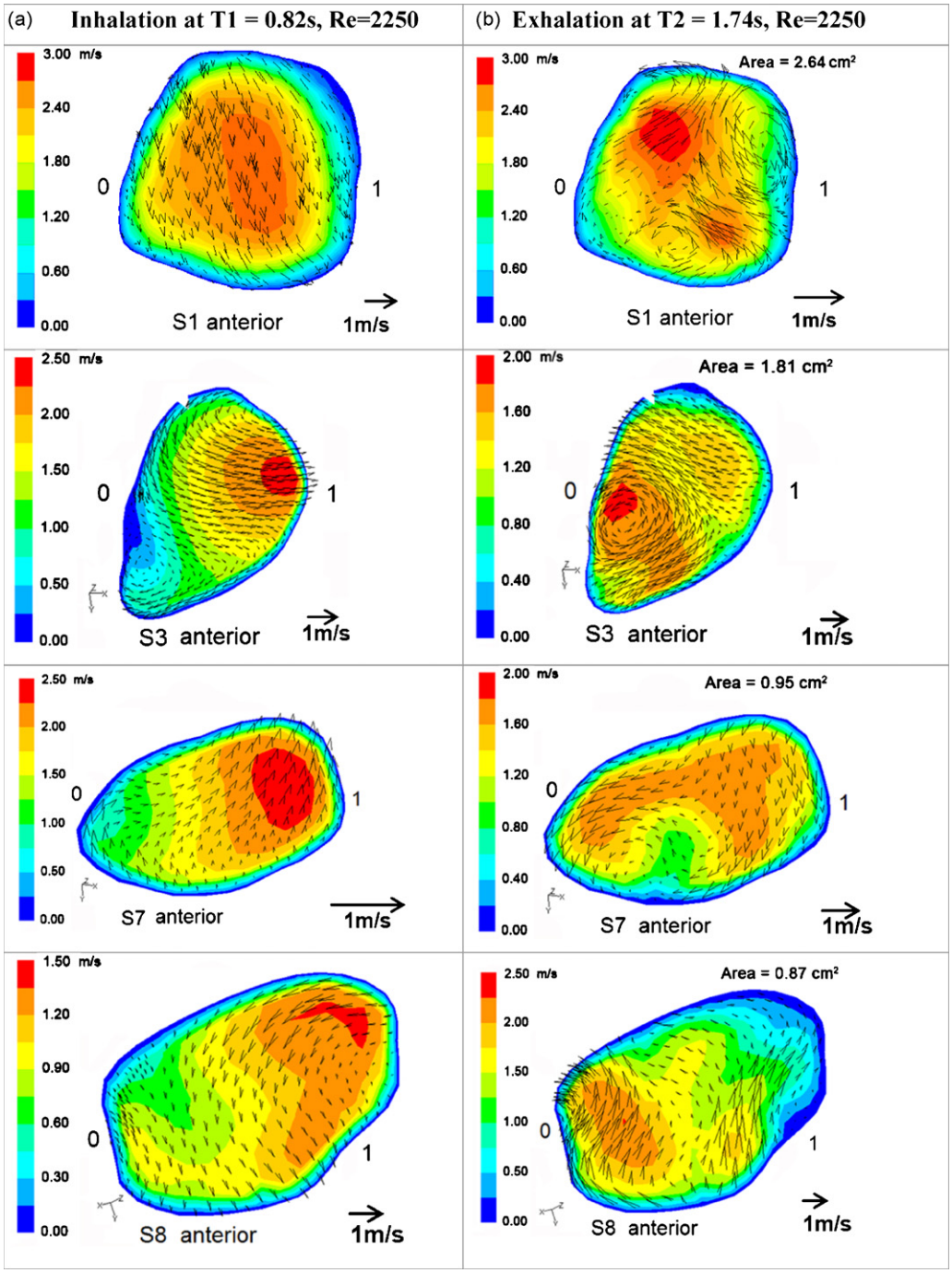

Fig. 8. (a) Velocity contours and secondary flow vector slices taken during inhalation at time $T1 = 0.82$ s and exhalation at time $T2 = 1.74$ s. Times are defined in Fig. 4b are taken for the RIGHT airway side as defined in Fig. 7a.

skewed direction is towards the inner walls of the second bifurcation. It can be seen that S5 is more highly skewed than S6 which is attributed to the upstream skewed profile as well as the high branching angle at the bifurcation.

In the right bronchi, a flat shaped profile at S7 was observed for the small branching angle and a less distorted upstream velocity field from the first bifurcation (i.e., S3). However it is noted that S8 is not as skewed as S5 despite S8 having a larger branching angle than S5. The branching angle at S5 was less than 90° (approx. 60° from the centre axis of left main bronchus), while at S8 the branching angle was approximately 90° which may affect the flow not in a distorted profile sense, but rather a greater reduction in the velocity magnitude. As an indication, axial velocity magnitude contours in Fig. 8 show that the right upper bronchi (S8) has a greater rate of reduction in maximum velocity than the left upper bronchi (S5) from their parent tubes (S3 and S4, respectively).

The flow features during the *exhalation phase* show different profiles. Instead of the airflow bifurcating during inhalation, a merging of the exhaled air into a single parent branch from the daughter branches (two or three in trifurcation, e.g., branch AIN = 111, the third right, upper trifurcation) occurs. The velocity profiles at the bifurcations naturally have indentations at the centres due to effects of merging coupled with the twists found in the airway geometry. In contrast to simple airway models [29,48,49], realistic airway models contain non-planar bifurcations where daughter tubes are often twisted which contribute to the indenta-

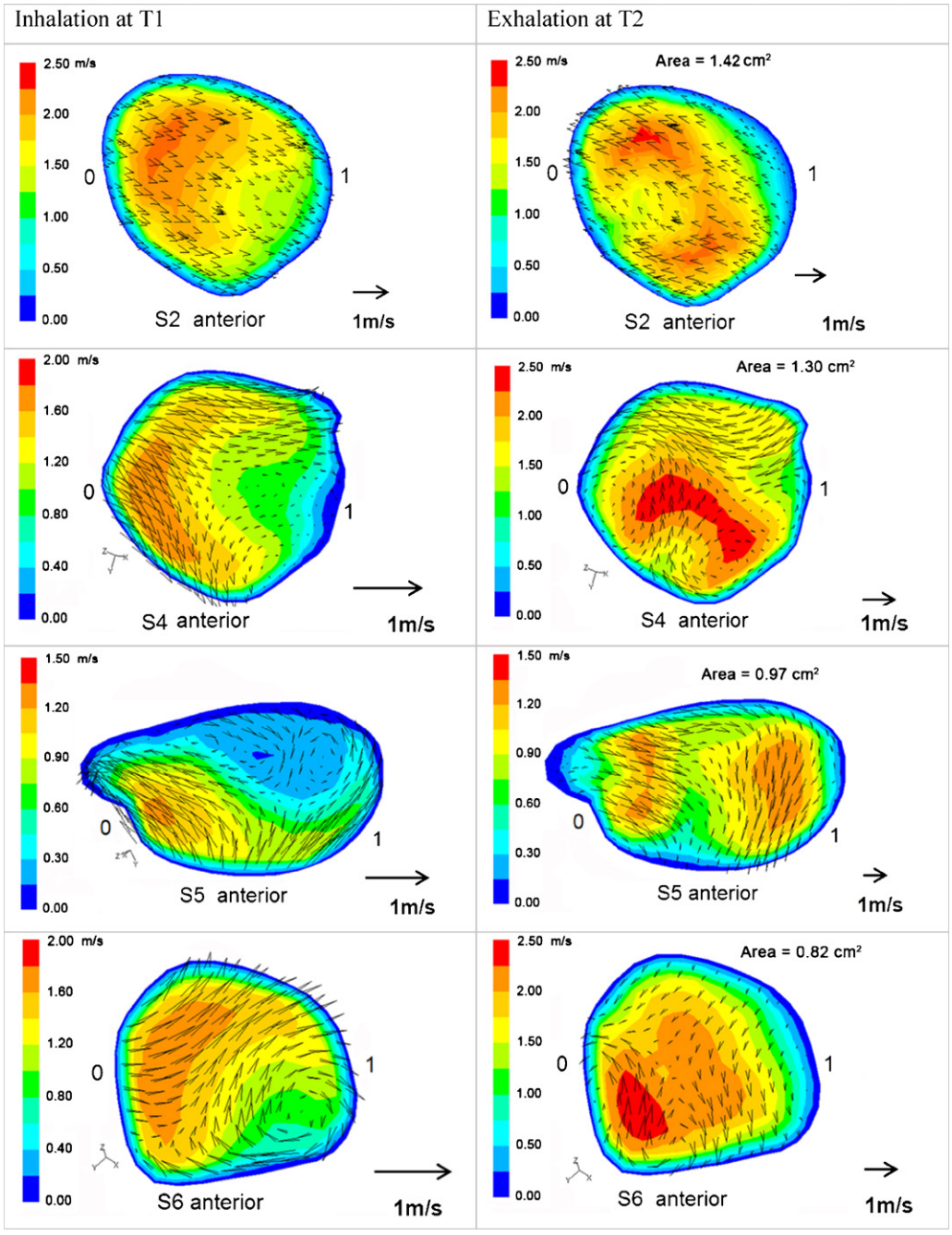

Fig. 9. (a) Velocity contours and secondary flow vector slices taken during inhalation at time $T1 = 0.82$ s and exhalation at time $T2 = 1.74$ s. Times are defined in Fig. 4b and the sections are taken for the LEFT airway side as defined in Fig. 7a.

tion at the centre of the axial velocity profile, causing an M-shaped profile. However, depending on the branching angle and the length and cross-sectional shape of daughter branches, this phenomenon did not necessary occur at some stations. S3, S5 and S6 in Fig. 7c showed that no indentations were observed at the given plane. This may be attributed to the large branching angle found at S3, where the upper daughter tube (S8) is perpendicular to the parent tube (S3) and the bottom tube (S7) is almost collinear to its parent tube.

In Figs. 8 and 9, secondary flow vectors overlayed onto axial velocity contour on selected cross-sections describe the flow phenomena in more detail. Firstly for the inhalation phase at $T1 = 0.82$ s, the secondary motion at the trachea just before the flow reaches the first bifurcation shows flow directed towards the anterior walls. When the flow reaches the right main bronchus (S3), two vortices appear as expected. This phenomenon has also been found by other researchers [9,17]. Axial velocity contours at S8 show high velocities close to the inner wall of the second bifurcation, whereas the high velocity region is found at the outer wall of S7. This can be explained by the principle of preferential flow distribution for daughter branches where a bias towards the smallest branching angle is achieved [17]. This also explains the magnitude scales at S7 which is larger than S8 and also in S5, S6 in Fig. 8. Recirculating flow in the form of vortices is found in S5 and S6. The vortex at S5 is weaker than the vortex at slice S6. In the left main bronchus, vortices are found at slices S2 and S4 which show strong motions travelling along the back of the slice as well as directing towards the front of the slice.

During the exhalation phase the flow changes direction which results in each daughter stream generating vortices. The resulting flow in the parent tube is the sum up of the vortices from its

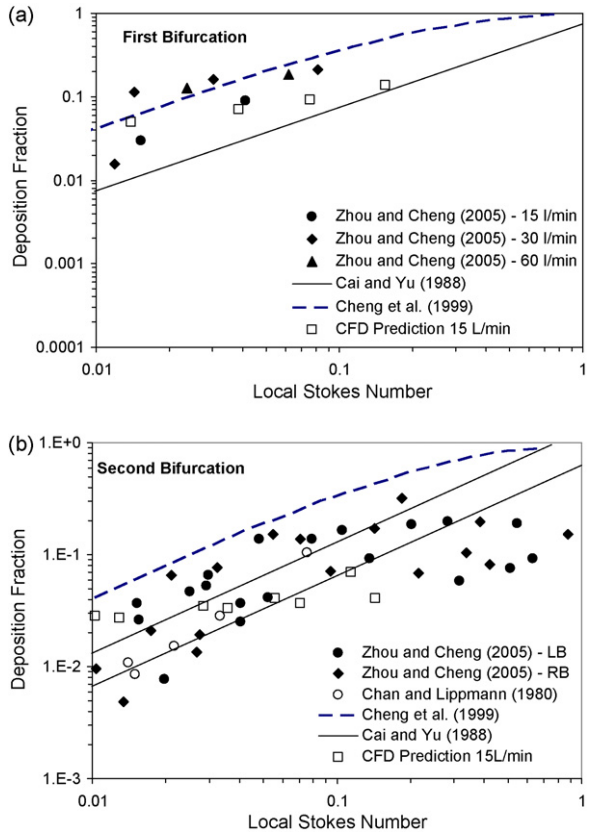

Fig. 10. Comparison of the CFD predicted deposition fraction versus reported lung cast deposition data, theoretical models and CFD predicted data at (a) the first bifurcation, and (b) the second bifurcation.

daughter tubes. S1 shows more vortices than its daughter tubes (S2 and S3). Likewise, slices at the left main bronchus (i.e., S2 and S4) showed how the vortices develop in a relatively long tube. The four vortices, resulting from the bulk flow develops upstream, but loses intensity as depicted by the length of the vectors. As previously mentioned, the branching angle and the length of the daughter tube can directly affect the indentations in axial velocity profile (M-shape) in the parent tube; similarly, secondary flow in the form of vortices is also influenced by the same factors. This can be seen in S3, S5–S8 where up to two vortices are weakly present in the slices. In terms of the streamlines' direction, the vectors during expiration were generally found to be in the opposite direction to the vectors during inspiration.

3.2. Particle deposition

In the following descriptions, the deposition fraction refers to the local deposition fraction in each individual branch. The total deposition fraction comparison is limited to the first two airway generations, and deposition in distal generations is not discussed, given the available data in the literature. The simulated results in the first bifurcation (Fig. 10a) generally lie between the theoretical models of Cheng et al. [37] and Cai and Yu [36]. The slope of CFD predictions is flatter than any of the data of Zhou and Cheng [21] which implies that greater differences in the deposition fraction are found as the particle size increases. The deposition mechanism of micron particle is dominated by inertial impaction (amongst sedimentation, interception and diffusion) which needs to be overcome in the first few branches for targeted drug delivery to deeper lung regions. This provides an explanation for the differences in comparison of the deposition pattern between the different airway models. For smaller particles with shorter relaxation times, the particles are able to adjust to flow streamlines more readily and hence the effect of different geometries is less significant. In contrast, larger particles with longer relaxation times are more likely to continue their own trajectory under their own inertia and thus, more likely to deviate from a curving streamline.

The CFD simulation results show an underprediction in comparison with the experimental data of Zhou and Cheng [21]. The lower deposition may be attributed to the computational models missing the larynx and the effects of the laryngeal jet, while the experimental model includes the oral cavity and the larynx. The laryngeal jet provides additional momentum and enhances the deposition fraction especially in the region at the beginning of the trachea. Current CT-scanning protocols must ensure patient safety and to obtain an accurate model, six generations deep prohibited the inclusion of the laryngeal region, due to long exposure times to radiation. The effects due to the exclusion of the larynx are most significant in the tracheal region and as the flow travels deeper into the airway, the effects begin to diminish.

The second bifurcation region includes the bifurcation of the right main bronchus (AIN = 11) and the left main bronchus (AIN = 12), and hence two bifurcations exist (Fig. 10b). The multiple lines for the empirical model of Cai and Yu [36] reflect the equivalent deposition fraction based on the different branch diameter and lengths for the left and right lung airway. The CFD predicted deposition fractions are compared with the experiment of Zhou and Cheng [21] and theoretical model of Cai and Yu [36]. In the medium Stokes number range of 0.07–0.2, the deposition fraction slope is consistent with the comparative data, while in the lower Stokes number range of <0.07 the deposition slope is much flatter than the comparative data. In the higher Stokes number range of >0.2, the experimental and theoretical data exhibit an inflexion point in the slope, which is not captured by the CFD results.

The deposition fraction for individual branches during the inhalation phase of the two breathing conditions is compared in Fig. 11. The increase in the total deposition fraction by inhalation for Case 1 is significantly higher (30.1% and 50.9% for 5 μm and 10 μm respectively) than for Case 2 (12.9% and 21.6% for 5 μm and 10 μm respectively) as a consequence of the higher inhalation rate increasing the particle inertia. In addition the 2 s breath hold time also becomes significantly important, allowing the particles to deposit by sedimentation rather than by inertial impaction. In Fig. 12 deposition by exhalation in individual branches during Case 2 breathing is shown to highlight the deposition contribution by inhalation and exhalation. It can be seen that the deposition fraction contribution from the exhalation phase increases for larger particles. For example in the deposition fraction during expiration in the first bifurcation contributed 15% of the final deposition fraction value for 10 μm particles, while for 5 μm particles the contribution during exhalation is 8%. This may be attributed to the merging of the branches, where the generation of vortices enhances the deposition of the particles. In the second bifurcation, at the right main bronchus (AIN = 11) more particles were captured when the breathing condition is by inhalation only (Fig. 11). However when exhalation is introduced the deposition fraction becomes much higher in the left main bronchus bifurcation (AIN = 12). The larger particle in this case magnifies this effect. In fact, the stronger secondary flow generated during exhalation at sections C and D (Figs. 8 and 9) leading to vortices in section D enhances the particle deposition. For brevity, the rest of the bifurcations showed that deposition fraction at exhalation could play a critical role in particle deposition, although how much of a proportion during expiration cannot be fully justified using the data provided here because lower generations of the airway are missing which can have an influence on the deposition fraction.

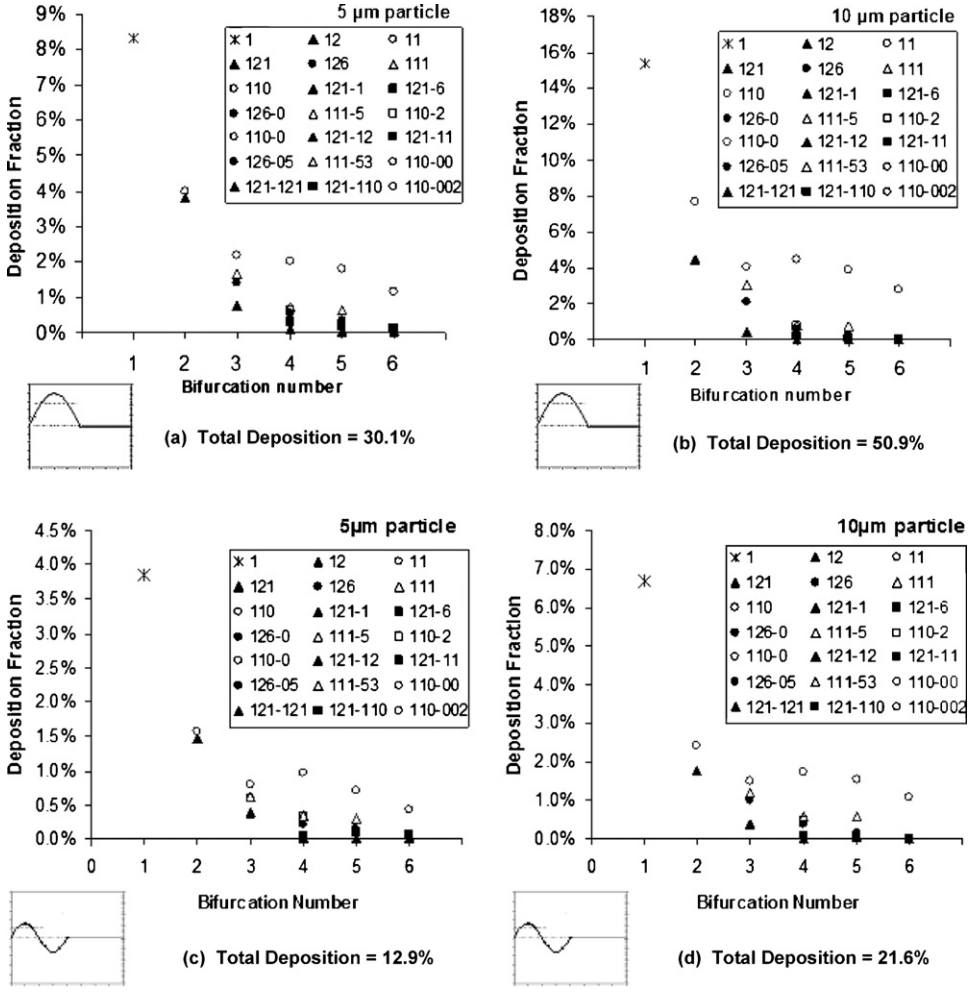

Fig. 11. Deposition fraction in each bifurcation for 5 μm and 10 μm for the entire breathing condition of Case 1 (a and b) and for the inhalation phase (first 1 s) only for Case 2 (c and d).

3.3. Deposition patterns

Deposition patterns on the three-dimensional airway model using the two breathing conditions, Case 1 and Case 2 were determined. There are several common findings for both cases in this particular model. The bend in the trachea just before the first bifurcation not only affected the flow profiles, but it also influenced the deposition pattern. This led to a higher concentration of particle deposition in the right side of the airway (Figs. 13 and 14). The particle deposition patterns for both particles sizes were qualitatively

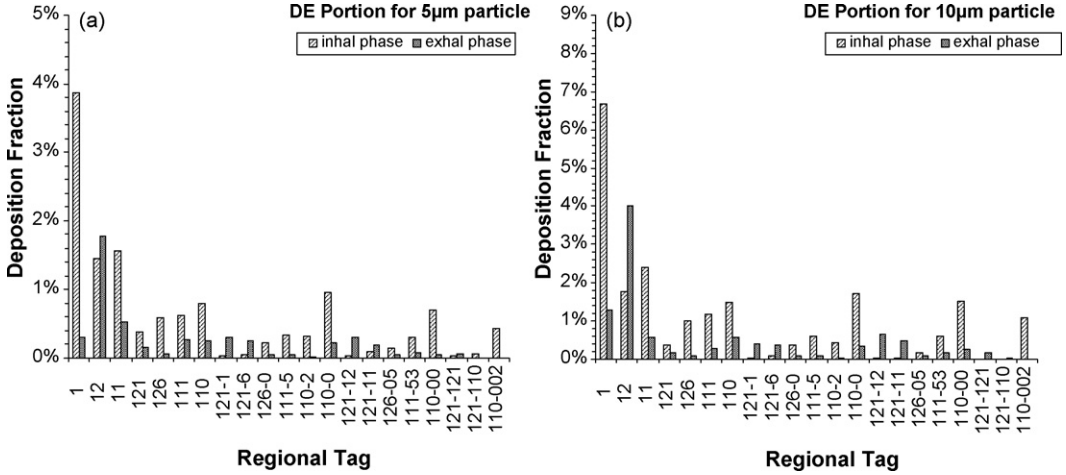

Fig. 12. Deposition fraction of particles in all bifurcations during inhalation and exhalation for particles of (a) 5 μm and (b) 10 μm in breathing Case 2. Note that the exhalation results represent only a fraction of the actual contribution to the total deposition under realistic breathing conditions, given that particles exiting the bifurcation model downstream upon inspiration will be deposited in the distal airways.

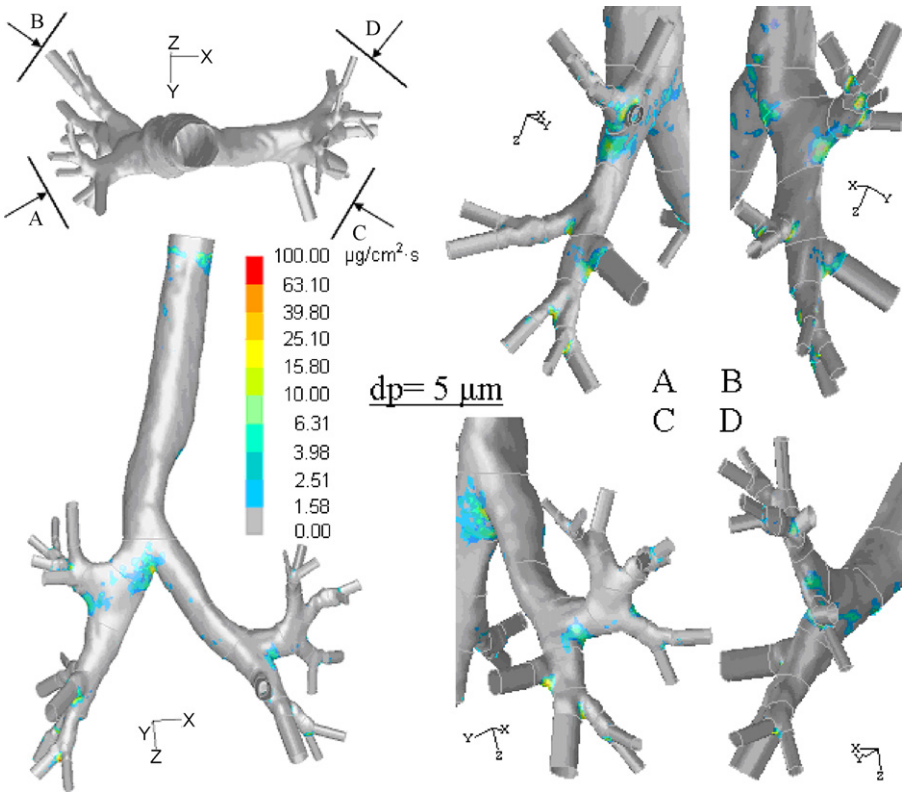

Fig. 13. Deposition patterns 5 μm particles ($St_{mean@inlet}$ = 0.03861 and $Re_{mean@inlet}$ = 5500) for breathing Case 1. Views A and B show enlarged views of right bronchus while Views C and D are the enlarged views of left bronchus.

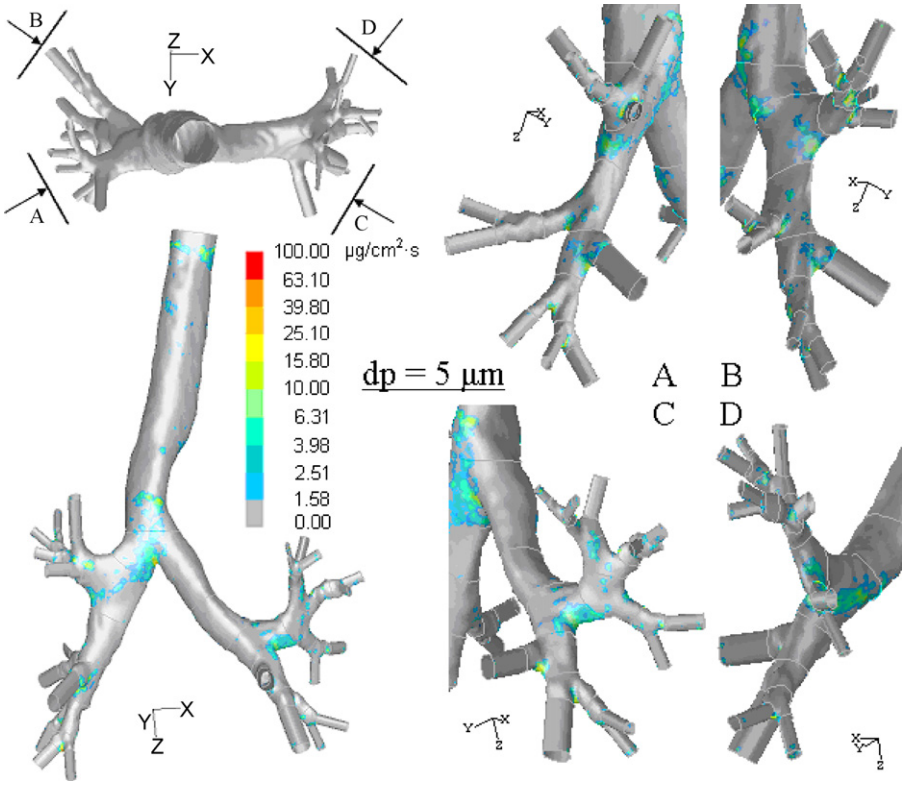

Fig. 14. Deposition patterns 5 μm particles ($St_{mean@inlet}$ = 0.01930 and $Re_{mean@inlet}$ = 2250) for breathing Case 2. Views A and B show enlarged views of right bronchus while Views C and D are the enlarged views of left bronchus.

similar and for brevity, only the deposition patterns for 5 μm are shown here. The main difference for the two different particle sizes was a slightly wider spread of particles and higher concentration values of localised "hot-spots" for the larger particle. However the locations of where the particles deposit are similar for both particle sizes. The deposition pattern for Case 1 can be predicted by analysing the secondary flow patterns during the inhalation phase in Figs. 8 and 9 since the secondary flow patterns during inhalation in Case 1 and Case 2 are identical. Due to the strong double vortices at S3 (Fig. 8, inhalation column), particles are concentrated at the inner wall of the first bifurcation. During exhalation particles were also transferred to the outer wall of the first bifurcation, but due to the relatively weaker movement of the flow, the concentration was not as high and not as widespread as found at the inner wall. This can be seen in the comparison of View B in Figs. 12 and 13. In general there is a tendency for the particles to deposit at the carina ridge.

The deposition patterns in Case 2 which are inclusive of the exhalation breathing phase show a greater surface area of deposition. Similarly it is the airflow patterns which are the inherent cause of the particle transport. The secondary flow vectors shown in S3 (Fig. 8, exhalation column) are directed towards the outer wall, enhancing deposition in this region. In addition it was shown in Fig. 12 that particle deposition from exhalation contributes to the total deposition fraction. A comparison of the deposition sites in the first bifurcation (View B) shows that some deposition occurs posteriorly for Case 2 but this deposition site is absent in Case 1. This is caused by the presence of a vortex generated from exhalation breath, which transports the particles to the posterior region of the tracheal bifurcation. Most of the particle deposition during exhalation was not only concentrated along carina ridges in the bifurcation but also downstream in the exhalation direction (upwards in the airway). The difference can be seen in the first bifurcation between the two cases (Figs. 13 and 14).

4. Discussion

Flow field analysis of secondary motion at the trachea just before the flow reaches the first bifurcation found the presence of several vortices during inhalation. In addition the there were vortices downstream as a result of the bifurcating flow for inhalation. During the exhalation phase the flow changes direction which results in each daughter stream generating vortices, and the resulting flow in the parent tube becomes the sum up of the vortices from its daughter tubes. In general the vortices during exhalation were weaker than for the inhalation. In terms of the streamlines' direction, the vectors during expiration were generally in the opposite direction to the vectors during inspiration, as a result of the opposing flow directions during the breathing cycle. It is expected that the increased effort in inhalation will magnify the vortices that are shown in Figs. 8 and 9. Therefore the flow field descriptions are useful for the understanding of the particles being transported through the airway. Breathing Case 1 is applicable to DPIs which require a high PIF for device activation, while breathing Case 2 can be applicable to pMDIs which require a slow steady inhalation. A lower PIF rate may not be able to produce drug particles fine enough to transport the particles into the TB tree given that the particles must traverse through the mouth and throat airway region. DPIs have the advantage that they have no propellant, and are easier to use than pMDIs. However the high PIF requirement can lead to early particle deposition (more so in the pharyngeal region) and treatment for very deep lung regions such as the acinus may not be achieved. The increased effort in breathing showed significantly higher deposition as expected because of the increase in the particle inertia. The breath hold after the initially high flow rate does however allow those particles suspended in the airway to settle and deposit by sedimentation. This is significant for the fine particles that can be produced that are able to follow the streamlines during any convective flow, to deposit by sedimentation. The combination of increased inhalation effort with breath hold, increased the deposition efficiency of 5 μm particles from 12.9% to 30.1% during normal inhalation only. The increased deposition efficiency is also found for 10 μm particle although this result is not as practical since the high inertia property of a 10 μm particle can prohibit its presence in the lung airways.

While most inhalers will deliver some of the drug to the main bronchi, treatment of respiratory diseases often requires particle deposition onto targeted specific sites such as the constricting bronchi caused by asthma, tumors, or in the deep lung regions (acinus). It is therefore evident that specific delivery devices are needed to achieve the particular desired effect. For example targeted delivery into the acinus lung region requires fine particles to be delivered through the device without such a high a PIF, in order to minimise the inertial impaction of the particles. Further developments in extending the geometry to include the mouth and larynx, and deeper into the lung airways past the sixth airway generation may be used to determine the extent of particle flow which was not captured in this study. The particles that escaped the limited domain may benefit from a longer settling time, and even the immediate exhalation following will increase the deposition.

Overall the deposition caused by exhalation was approximately 50% to that of inhalation. The particles are largely concentrated in the first few bifurcations despite the exhalation phase. In addition the deposition patterns showed that the deposition is located at the carina at each bifurcation. This suggests that the deposition mechanism is dominantly by inertial impaction (amongst sedimentation, interception and diffusion) which needs to be overcome in the first few branches for targeted drug delivery to deeper lung regions. In general the right airway side captured more particles than the left side which may be due to: the relatively large diameter branches in the right side which reduces the airflow velocity; and the branching angles of the daughter branches which in most lung airway cases is biased towards the trachea-AIN11 branch (right lung). Inter-individual variations amongst subjects exist between all models, however understanding the gross flow features such as the dominance towards the right lung can help guide new and novel delivery methods such as guided drug delivery [50,51].

4.1. Limitations of this study

Several assumptions were made when carrying out this analysis which limited the degree to which the present work can be extrapolated to real world scenarios. One such limitation is the representativeness of the computational model which was reconstructed from CT scans of a 53-year-old non-smoking Caucasian female. Thus the results are limited to similar anatomical subjects. Also, in terms of simulation, a fully developed profile was used at the trachea inlet and the airway outlets. In anatomical and physiological terms, the larynx and additional lower branch generations were excluded and thus, the larynx effect and effects of the upstream flow for inhalation and exhalation were not included. The input waveform was simplified as a sinusoidal wave which may have an effect on the particle deposition fraction and patterns; however, there are few studies on this matter, so the effect of the input waveform may be studied in the future. For the particle analysis, deposition occurring upstream of the trachea is not considered because of the geometry limitation. Physically the particles are introduced at the mouth and must pass through the larynx before entering the trachea. Therefore the particle deposition given in this study is the deposition fraction relative to the number of particles that reach the trachea.

5. Conclusion

Velocity profiles, local deposition fraction and deposition patterns of aerosol particles in the first six generations of an airway model were simulated. Two realistic inhalation conditions were applied to study the particle-fluid interactions. Deposition patterns were used to illustrate local deposition regions in the airway that highlighted the differences between the two breathing conditions—specifically the different inhalation conditions. Velocity profiles were also used to analyse the deposition pattern forming. From a deposition efficiency perspective, a deep inhalation with a breath hold of 2 s did not necessarily increase later deposition up to the sixth branch generation, but rather increase in the deposition in the first few airway generations was found. In certain conditions, complete cyclic breaths with high frequency can enhance the transportation of aerosols to the same location. A short tidal breath with a small air volume gave a lower total deposition fractions in the first six generations during the inhalation phase (5 μm = 12.9%; 10 μm = 21.6%) when compared with a single deeper inhalation and breath hold (5 μm = 30.1%; 10 μm = 50.9%). This finding can be further refined by incorporating the percentage of aerosols that may be captured by the lower generations (after sixth generation) during expiration, which may affect the results to a certain extent. Furthermore, individuals display unique airway geometries and it is important to evaluate the particle deposition pattern and particle density accordingly in order to provide accurate inhalation risk or dose–response assessment. This study demonstrated that CFD is capable of providing insight into fluid-particle dynamics and visualising particle deposition for health risk assessment and/or clinical assessment using the realistic human airway models.

Acknowledgements

The financial support provided by the Australian Research Council (project ID LP0989452) and by RMIT University through an Emerging Research Grant is gratefully acknowledged.

Conflict of interest statement

The authors hereby declare that this paper has not been influenced by any conflict of interest. This includes no financial or personal relationships with external parties that would influence the work.

References

[1] Virchow JC, Crompton GK, Dal Negro R, Pedersen S, Magnan A, Seidenberg J, et al. Importance of inhaler devices in the management of airway disease. Respiratory Medicine 2008;102(1):10–9, doi:10.1016/j.rmed.2007.07.031.
[2] Lenney J, Innes JA, Crompton GK. Inappropriate inhaler use: assessment of use and patient preference of seven inhalation devices. Respiratory Medicine 2000;94(5):496–500, doi:10.1053/rmed.1999.0767.
[3] Larsen JS, Hahn M, Ekholm B, Wick KA. Evaluation of conventional press-and-breathe metered-dose inhaler technique in 501 patients. Journal of Asthma 1994;31(3):193–9.
[4] De Boeck K, Alifier M, Warnier G. Is the correct use of a dry powder inhaler (Turbohaler) age dependent? Journal of Allergy and Clinical Immunology 1999;103(5):763–7, doi:10.1016/S0091-6749(99)70417-3.
[5] Lavorini F, Magnan A, Christophe Dubus J, Voshaar T, Corbetta L, Broeders M, et al. Effect of incorrect use of dry powder inhalers on management of patients with asthma and COPD. Respiratory Medicine 2008;102(4):593–604, doi:10.1016/j.rmed.2007.11.003.
[6] Jackson C, Lipworth B. Optimizing inhaled drug delivery in patients with asthma. British Journal of General Practice 1995;45:683–7.
[7] Dalby R, Suman J. Inhalation therapy: technological milestones in asthma treatment. Advanced Drug Delivery Reviews 2003;55(7):779–91.
[8] Proetz AW. Air currents in the upper respiratory tract and their clinical importance. The Annals of Otology, Rhinology, and Laryngology 1951;60:439–67.
[9] Schroter RC, Sudlow MF. Flow patterns in models of the human bronchial airways. Respiration Physiology 1969;7.(341–355).
[10] Chang HK, El Masry OA. A model study of flow dynamics in human central airways. Respiration Physiology 1982;49(1):75–95.
[11] Isabey D, Chang HK. Steady and unsteady pressure-flow relationships in central airways. Journal of Applied Physiology 1981;51:1338–48.
[12] Weibel ER. Morphometry of the human lung. New York, US: Academic Press; 1963.
[13] Horsfield K, Gladys D, Olson DE, Finlay GF, Cumming G. Models of the human bronchial tree. Journal of Applied Physiology 1971;31(2):207–17.
[14] van Ertbruggen C, Hirsch C, Paiva M. Anatomically based three-dimensional model of airways to simulate flow and particle transport using computational fluid dynamics. Journal of Applied Physiology 2005;98:970–80.
[15] Kim CS, Hu SC, Dewitt P, Gerrity TR. Assessment of regional deposition of inhaled particles in human lungs by serial bolus delivery method. Journal of Applied Physiology 1996;81:2203–13.
[16] Perzl MA, Schultz H, Parezke HG, Englmeier KH, Heyder J. Reconstruction of the lung geometry for the simulation of aerosol transport. Journal of Aerosol Medicine 1996;9:409–18.
[17] Vial L, Perchet D, Fodil R, Caillibotte G, Fetita C, Preteux F, et al. Airflow modeling of steady inspiration in two realistic proximal airway trees reconstructed from human thoracic tomodensitometric images. Computer Methods in Biomechanics and Biomedical Engineering 2005;8:267–77.
[18] Lippman M, Yeates DB, Albert RE. Deposition, retention and clearance of inhaled particles. Journal of Industrial Medicine 1993;37:337–62.
[19] Matthys H. Inhalation delivery of asthma drugs. Lung 1990;1990(Suppl.):645–52.
[20] Tschirren J, Hoffman EA, McLennan G, Sonka M. Segmentation and quantitative analysis of intrathoracic airway trees from computed tomography images. Proceedings of the American Thoracic Society 2005 December 1;2(6):484–7.
[21] Zhou Y, Cheng YS. Particle deposition in a cast of human tracheobronchial airways. Aerosol Science and Technology 2005;39:492–500.
[22] Sauret V, Halson PM, Brown IW, Fleming JS, Bailey AG. Study of the three-dimensional geometry of the central conducting airways in man using computed tomographic (CT) images. Journal of Anatomy 2002;200:123–34.
[23] Mortensen JD, Young JD, Stout L, Stout A, Bagley B, Schaap RN. A numerical identification system for airways in the lung. The Anatomical Record 1983;206:103–14.
[24] Broeders ME, Molema J, Vermue NA, Folgering HT. Peak inspiratory flow rate and slope of inhalation profiles in dry powder inhalers. European Respiratory Journal 2001;18:780–3.
[25] Srichana T, Martin GP, Marriott C. Dry powder inhalers: the influence of device resistance and powder formulation on drug and lactose deposition in vitro. European Journal Pharmaceutical Science 1998;7:73–80.
[26] Balashazy I, Hofmann W. Particle deposition in airway bifurcations—I. Inspiratory flow. Journal of Aerosol Science 1993;24(6):745–72.
[27] Longest PW, Vinchurkara S, Martonen T. Transport and deposition of respiratory aerosols in models of childhood asthma. Aerosol Science 2006;37:1234–57.
[28] Zhang Z, Kleinstreuer C. Effect of particle inlet distributions on deposition in a triple bifurcation lung airway model. Journal of Aerosol Medicine—Deposition Clearance and Effects in the Lung 2001;14(1):13–29.
[29] Zhang Z, Kleinstreuer C, Kim CS. Flow structure and particle transport in a triple bifurcation airway model. Journal of Fluids Engineering—Transactions of the ASME 2001;123(2):320–30.
[30] Li Z, Kleinstreuer C, Zhang Z. Simulation of airflow fields and microparticle deposition in realistic human lung airway models. Part I. Airflow patterns. European Journal of Mechanics B/Fluids 2007;26:632–49.
[31] Zhang Z, Kleinstreuer C, Donohue JF, Kim CS. Comparison of micro- and nano-size particle depositions in a human upper airway model. Journal of Aerosol Science 2005;36:211–33.
[32] Chan TL, Schreck RM, Lippman M. Effect of the laryngeal jet on particle deposition in the human trachea and upper bronchial airways. Journal of Aerosol Science 1980;11(5–6):447–59.
[33] Takano H, Nishida N, Itoh M, Hyo N, Majima Y. Inhaled particle deposition in unsteady-state respiratory flow at a numerically constructed model of the human larynx. Journal of Aerosol Medicine 2006;19(3):314–28.
[34] Xi J, Longest PW, Martonen TB. Effects of the laryngeal jet on nano- and microparticle transport and deposition in an approximate model of the upper tracheobronchial airways. Journal of Applied Physiology 2008 June 1;104(6):1761–77.
[35] Edwards DA. Delivery of biological agents by aerosols. AIChE Journal 2002;48:2–6.
[36] Cai FS, Yu CP. Inertial and interceptional deposition of spherical particles and fibres in a bifurcating airway. Journal of Aerosol Science 1988;19(6):679–88.
[37] Cheng YS, Zhou Y, Chen BT. Particle deposition in a cast of human oral airways. Aerosol Science and Technology 1999;31(4):286–300.
[38] Zhang Y, Finlay WH. Measurement of the effect of cartilaginous rings on particle deposition in a proximal lung bifurcation model. Aerosol Science and Technology 2005;39:394–9.
[39] Zhang Z, Kleinstreuer C. Modeling of low Reynolds number turbulent flows in locally constricted conduits: a comparison study. AIAA Journal 2003;41:831–40.
[40] Varghese SS, Frankel SH. Numerical modeling of pulsatile turbulent flow in stenotic vessels. ASME Journal of Biomechanical Engineering 2003;123:445–60.

[41] Wilcox D. Turbulence modeling for CFD. 5354 Palm Drive, La Canada, California 91011: DCW Industries, Inc.; 1993.
[42] Morsi SA, Alexander AJ. An investigation of particle trajectories in two-phase flow systems. Journal Fluid Mechanics 1972;55(2):193–208.
[43] Matida EA, Finlay WH, Lange CF, Grgic B. Improved numerical simulation fo aerosol deposition in an idealized mouth-throat. Journal of Aerosol Science 2004;35:1–19.
[44] Dehbi A. Turbulent particle dispersion in arbitrary wall-bounded geometries: a coupled CFD–Langevin-equation based approach. International Journal of Multiphase Flow 2008;34(9):819–28.
[45] Inthavong K, Tian ZF, Li HF, Tu JY, Yang W, Xue CL, et al. A numerical study of spray particle deposition in a human nasal cavity. Aerosol Science and Technology 2006;40(11):1034–45.
[46] Menon AS, Weber ME, Chang HK. Model study of flow dynamics in human central airways. Part III. Oscillatory velocity profiles. Respiration Physiology 1984;55:255–75.
[47] Comer JK, Kleinstreuer C, Zhang Z. Flow structures and particle deposition patterns in double-bifurcation airway models. Part 1. Air flow field. Journal of Fluid Mechanics 2001;435:25–54.
[48] Lee JW, Goo JH, Chung MK. Characteristics of inertial deposition in a double bifurcation. Journal of Aerosol Science 1996;27(1):119–38.
[49] Zhao Y, Lieber BB. Steady inspiratory flow in a model symmetric bifurcation. Journal of Biomechanical Engineering 1994;116:488–96.
[50] Saiyed Z, Telang S, Ramchand C. Application of magnetic techniques in the field of drug discovery and biomedicine. BioMagnetic Research and Technology 2003;1(1):2.
[51] McCarthy JR, Kelly KA, Sun EY, Weissleder R. Targeted delivery of multifunctional magnetic nanoparticles. Nanomedicine 2007;2(2):153–67.
[52] Kelly JT, Asgharian B, Kimbell JS, Wong BA. Particle deposition in human nasal airway replicas manufactured by different methods. Part 1. Inertial regime particles. Aerosol Science and Technology 2004;38:1063–71.
[53] Cheng YS, Holmes TD, Gao J, Guilmette RA, Li S, Surakitbanharn Y, Rowlings C. Characterization of nasal spray pumps and deposition pattern in a replica of the human nasal airway. Journal of Aerosol Medicine 2001;14: 267–80.
[54] Shi HW, Kleinstreuer C, Zhang Z. Modeling of inertial particle transport and deposition in human nasal cavities with wall roughness. Journal of Aerosol Science 2007;38:398–419.